

Electrospun membranes chelated by metal magnesium ions enhance pro-angiogenic activity and promote diabetic wound healing

Mingyue Liu^{a,1}, Xiaoyi Wang^{b,1}, Binbin Sun^a, Hongsheng Wang^a, Xiumei Mo^a, Mohamed EL-Newehy^c, Meera Moydeen Abdulhameed^c, Haochen Yao^{d,*}, Chao Liang^{e,*}, Jinglei Wu^{a,*}

^a Shanghai Engineering Research Center of Nano-Biomaterials and Regenerative Medicine, Department of Biomedical Engineering, Donghua University, Shanghai 201620, PR China

^b Core Facility Center, The First Affiliated Hospital of Nanjing Medical University, Nanjing 210029, PR China

^c Department of Chemistry, College of Science, King Saud University, P.O. Box 2455, Riyadh 11451, Saudi Arabia

^d Department of Hepatobiliary and Pancreatic Surgery, General Surgery Center, First Hospital of Jilin University, Changchun 130021, China

^e Department of Urology, The First Affiliated Hospital of Nanjing Medical University, Nanjing 210029, PR China

ARTICLE INFO

Keywords:

Electrospinning
Magnesium ion
Nanofiber membrane
Diabetic wounds
Wound dressing

ABSTRACT

Diabetic wounds, resulting from skin atrophy due to localized ischemia and hypoxia in diabetic patients, lead to chronic pathological inflammation and delayed healing. Using electrospinning technology, we developed magnesium ion-chelated nanofiber membranes to explore their efficacy in antibacterial, anti-inflammatory, and angiogenic applications for wound healing. These membranes are flexible and elastic, resembling native skin tissue, and possess good hydrophilicity for comfortable wound bed contact. The mechanical properties of nanofiber membranes are enhanced by the chelation of magnesium ions (Mg^{2+}), which also facilitates a long-term slow release of Mg^{2+} . The cytocompatibility of the nanofibrous membranes is influenced by their Mg^{2+} content: lower levels encourage the proliferation of fibroblasts, endothelial cells, and macrophages, while higher levels are inhibitory. In a diabetic rat model, magnesium ion-chelated nanofibrous membranes effectively reduced early wound inflammation and notably accelerated wound healing. This study highlights the potential of magnesium ion-chelated nanofiber membranes in treating diabetic wounds.

1. Introduction

Nearly 500 million people worldwide are estimated to suffer from diabetes mellitus (DM), with the expected number rising alarmingly in the coming years. In the United States alone, diabetes accounts for over \$300 billion annually in medical costs and lost workdays [1,2]. Approximately 20 % of diabetic patients are likely to develop chronic non-healing wounds, such as diabetic foot ulcers, in their lifetime. These ulcers have high recurrence rates, with 40 % recurring within one year and 65 % within five years. Unfortunately, there is no effective treatment for diabetic foot ulcers [3,4]. Two main events effectively promote wound healing including the inflammatory response and the migration of cells (keratinocytes, fibroblasts, and endothelial cells), but these are dysregulated for diabetic patients [5]. There is a significant reduction in fibroblast proliferation, function, and differentiation into

myofibroblasts. DM also disrupts re-epithelialization and protein synthesis and inhibits the migration and proliferation of keratin-forming cells and fibroblasts [6–9]. Additionally, DM results in dysregulated expression of several keratin-forming cell proteins associated with re-epithelialization, including cytoskeletal keratin proteins (K2, K6, and K10), which are essential for keratin-forming cell differentiation and epithelial cell binding to the basement membrane [10]. Subsequently, the reduction in keratin-forming cell proteins affects the survival and differentiation of those effector cells, resulting in impaired wound re-epithelialization [11].

Clinical management of chronic wounds includes skin perfusion restoration, infection treatment, metabolic control, treatment of coexisting conditions, and local wound care [12]. Despite the significant progress of wound dressing materials in recent years, challenges remain for diabetic wound treatments. Traditional treatments, mainly involving

* Corresponding authors.

E-mail addresses: yaohaochen@jlu.edu.cn (H. Yao), cliang@njmu.edu.cn (C. Liang), jw@dhu.edu.cn (J. Wu).

¹ These authors contributed equally to this work.

dressings, are lengthy, risk secondary injuries, and cause psychological and physiological stresses to diabetic patients. Additionally, diabetic wounds often require extended healing periods due to persistent inflammation, bacterial infection, and dysregulated growth factor degradation or expression [13]. Chronic hyperglycemia hinders capillary formation, limiting oxygen and nutrient access to wound sites [14]. These necessitate multifunctional dressing materials that are biologically active in anti-inflammatory and antibacterial to enhance diabetic wound healing.

Electrospinning represents one of the simplest technologies to generate nanofiber membranes with structures similar to the native extracellular matrix. Electrospun nanofiber membranes can effectively cover and protect wounds owing to their softness and compliance [15–17]. To reduce infection and promote wound healing, therapeutic agents have been incorporated into electrospun nanofibers. Commonly used antibacterial agents and growth factors include antibiotics [18], antibacterial peptides [19], inorganic nanoparticles [20], and transforming growth factors [21]. Among these therapeutic agents, inorganic nanoparticles have attracted increasing attentions due to their unique antibacterial capacity and/or bioactivity. Current inorganic nanoparticles used for wound healing include silver [22–24], gold, copper [25], magnesium oxide (MgO), and bioactive glass [14,26–30]. MgO nanoparticles are unique in promoting wound healing due to their unique anti-inflammatory and antibacterial activities. Our previous studies have shown that MgO-incorporated nanofiber membranes were beneficial for wound healing [31–34]. However, there was an inherent limitation for MgO-incorporated nanofiber membranes associated with the burst release of inorganic nanoparticles, which alter the local pH of wounds and lead to short-term toxicity to the body. In addition, the aggregation of MgO nanoparticles within nanofibers compromises the mechanical properties of electrospun membranes.

In this study, we proposed a method to prepare magnesium ion-chelated nanofiber membranes and investigated their capacity as dressing materials for diabetic wound treatment. MgO nanoparticles were converted into magnesium acetate (MgAC) during the preparation of electrospun solutions, where appropriate amounts of acetic acid were added into polycaprolactone (PCL)/gelatin solutions. This conversion allowed the homogenous distribution of MgAC within nanofibers and significantly improved their physicochemical properties and biological performance. Physicochemical properties of these MgAC-incorporated membranes were characterized and their cytocompatibility, bioactivity, and hemostatic properties *in vitro*, as well as antibacterial activity, were assessed. Finally, PCL/gelatin/MgAC nanofiber membranes were used as dressings in a diabetic rat model to assess their capacity to promote diabetic wound healing.

2. Materials and methods

2.1. Materials

PCL (M_n 80 kDa) and type A gelatin (~300 g Bloom) were purchased from Sigma-Aldrich. Glacial acetic acid, 2,2,2-trifluoroethanol (TFE), and magnesium oxide nanoparticles (MgO, ~50 nm diameter) were obtained from Shanghai Aladdin Bio-Chem Technology Co., LTD. Streptozotocin (STZ) and sodium citrate were provided by Shanghai Macklin Biochemical Co., Ltd. All chemicals were used as received without purification.

2.2. Preparation of MgAC-incorporated electrospun membranes

PCL and gelatin were dissolved in TFE at the polymer concentration of 10 % (wt/v) with a PCL/gelatin ratio of 8:2, as described elsewhere [34]. Various amounts (0.5 % to 2 %, wt/v) of MgO nanoparticles were added to the as-prepared PCL/gelatin solutions and sonicated for 30 min to fully disperse the nanoparticles. Subsequently, excess acetic acid was added to electrospun solutions and stirred at room temperature for 24 h.

The molar ratio of acetic acid/MgO was 2.5:1 to completely convert MgO nanoparticles into MgAC. The PCL/gelatin/MgAC solutions were fed at 2 mL/h and electrospun at a high voltage of 16 kV and collected by a mandrel (100 rpm) at a distance of 10 cm. Electrospun nanofiber membranes prepared from formulations by adding 0.5 %, 1 %, and 2 % (wt/v) MgO nanoparticles in PCL/gelatin solutions were denoted as MgAC-0.5, MgAC-1, and MgAC-2, respectively. Electrospun membranes made from PCL/gelatin solutions without the addition of MgO nanoparticles but with acetic acid (0.2 %, v/v) were denoted as PCL/gelatin and served as a control.

2.3. Characterization of MgAC-incorporated electrospun membranes

Surface morphology and chemical compositions of electrospun membranes were analyzed by a scanning electron microscope (SEM, Hitachi, TM-1000, Japan) with an ESM spectrometer. Fiber diameters of electrospun membranes were measured from SEM images using ImageJ. The chemical structure and crystalline phase of electrospun membranes were determined by Fourier transform infrared spectroscopy (FTIR) and X-ray diffraction (XRD), respectively. Briefly, attenuated total reflection mode of a Nicolet-760 FTIR spectrometer was used to collect the wavelength of electrospun membranes at the range of 4000 cm^{-1} – 400 cm^{-1} . For XRD analysis, a Bruker AXS D8 Discover X-ray diffractometer was used to detect the crystalline phase of electrospun membranes at a 2θ degree between 10° and 60° . Thermogravimetric analysis (TGA) of electrospun membranes was conducted using a Libra 209F1 TGA (Selb, Germany) at a scan rate of $20^\circ\text{C}/\text{min}$ from 100°C to 700°C under an inert atmosphere.

The surface hydrophobicity of electrospun membranes was assessed by an SL200A contact angle analyzer (Solon Tech., Shanghai, China). A droplet of 5 μL deionized water was dropped onto the membrane surface and videoed until the droplet disappeared. Images at 5 s were retrieved and used to calculate the contact angle for each sample. A tangent line of the droplet on the sample surface was made to determine the contact angle of MgAC-incorporated electrospun membranes ($n = 3$). The pH changes and cumulative release of Mg^{2+} from MgAC-incorporated membranes were tested by incubating samples in saline at 37°C . The dissolution rate of the electrospun membrane was evaluated by measuring the water absorption of the electrospun membrane. The pH values of electrospun membrane incubations were measured using a digital pH meter ($n = 4$). At predesigned time points, the incubation solution was collected for analysis and an equal volume of fresh saline was added. The concentration of magnesium ions in each group of samples ($n = 4$) was determined by an inductively coupled plasma atomic emission spectroscopy (ICP-AES) (Prodigy Plus, Teledyne Leeman Labs, USA). To better mimic the body fluid pH microenvironment of normal and diabetic rats, we also evaluated the magnesium ion release rate from nanofiber membranes in solutions at pH of 5 and 8. Simultaneously, we evaluated the degradation rates of nanofiber membranes in solutions with pH 5 and 8.

Electrospun membranes were tailored into strip specimens ($10 \times 40\text{ mm}$) and incubated in saline at 37°C for 12 h for uniaxial tensile tests. Specimens were mounted in the grips of a universal materials testing machine (Instron 5567, Norwood, MA) with a 200 N load cell and were tested at a crosshead speed of 10 mm/min until failure. Ultimate tensile strength (UTS) was determined by the maximum tensile strength before the sample breaks and Young's modulus was calculated as the slope of the initial 5 % linear portion from the stress-strain curve ($n = 6$).

2.4. Cytocompatibility and cell behaviors

Cytocompatibility of electrospun membranes was assessed with key cells participating in wound healing process. Human umbilical vein endothelial cells (HUVECs) and human foreskin fibroblast (HFF) were provided by the Stem Cell Bank, Chinese Academy of Sciences (Shanghai). Electrospun membranes were punched to discs and

disinfected with 70 % ethanol for 1 h and then irradiated under UV (12 h for each side) before cell seeding. Cells were seeded on the surface of membranes at various densities for different studies. Cell-seeded membranes were maintained in high glucose Dulbecco's Modified Eagle medium (DMEM) supplemented with 10 % fetal bovine serum and 1 % penicillin/streptomycin antibiotics in a 37 °C incubator with 95 % humidity and 5 % CO₂. The medium was refreshed every other day. HUVEC and HFF were seeded at a density of 5.0×10^4 cells/well in 48-well plates. Cell viability and proliferation on electrospun membranes in 48 well plates were assessed by live/dead staining and CCK-8 assay, respectively. At days 1, 4, and 7, cell-seeded membranes were stained with calcein-AM and propidium iodide for 30 min at 37 °C and visualized using a fluorescence microscope (DMi 8, Leica, Germany) ($n = 3$). For proliferative assessment, cell-seeded membranes were incubated with CCK-8 assay at 37 °C for 2 h, and then 100 μ L supernatant of each well was read at 450 nm using a plate reader (Multiskan MK3, Thermo, USA) ($n = 4$). Cell-seeded membranes were rinsed with PBS, fixed with 4 % paraformaldehyde, dehydrated with graded ethanol, dried at room temperature, sputtered with gold, and observed by SEM.

To determine vascular endothelial growth factor (VEGF) accumulation, HUVECs were seeded at a density of 1×10^5 cells/well on electrospun membranes in 24-well plates. At day 7, cell culture medium was collected to measure accumulated VEGF using ELISA kit (Invitrogen) following manufacturer's instructions ($n = 4$). Fibroblasts were seeded on electrospun membranes at a density of 3×10^5 cells/well in a 12-well plate to quantify the amounts of cell-secreted transforming growth factor- β 1 (TGF- β 1). Accumulated TGF- β 1 was measured by ELISA kit (Invitrogen) following manufacturer's instructions ($n = 4$).

2.5. Blood clotting and hemolysis ratio

A dynamic whole blood coagulation assay was used to evaluate the *in vitro* hemostatic ability. Electrospun membranes were punched to 14 mm discs and pre-warmed at 37 °C for 10 min. Then, 100 μ L fresh anticoagulant rabbit whole blood solution (0.2 M CaCl₂, 10 mM in the blood) was dropped onto the surface of membranes and incubated in a shaker (50 rpm) at 37 °C to allow interaction between blood and nanofibers. Then 10 mL deionized (DI) water was slowly added to release the unbound blood without interfering with the clot and incubated in a shaker (50 rpm) at 37 °C for 5 min to collect the free erythrocytes. The absorbance of 100 μ L fresh anticoagulant rabbit whole blood solution in 10 mL DI water was used as the negative control. The commercial gauze was used as a control group. 100 μ L hemoglobin solution of each sample was read at 540 nm using a plate reader (Multiskan MK3, Thermo, USA) ($n = 3$). The blood-clotting index (BCI) was calculated using the equation:

$$BCI (\%) = [(I_s - I_o)/(I_r - I_o)] \times 100\%$$

where I_s represents the absorbance of the sample, I_r represents the absorbance of the negative control group and I_o represents the absorbance of the reference value.

The whole blood clotting time was tested according to previous studies [35]. Briefly, 2 mL of whole blood (containing 10 % sodium citrate) was added into a sample tube containing 10 mg of each membrane and 60 μ L of CaCl₂ (0.25 mol/L) solution. Clotting time for each sample was recorded ($n = 3$).

The *in vitro* hemolysis rate was tested with 2 % (v/v) erythrocytes suspension. Briefly, fresh anticoagulated whole blood (2 mL) diluted in saline (5 mL) was taken and centrifuged at 3000 rpm for 10 min. The obtained erythrocytes were further diluted to 2 % (v/v). Various equal-mass membranes were pre-warmed in normal saline at 37 °C for 30 min, and then the diluted erythrocyte suspension (0.2 mL) was dropped into the above samples. After incubation at 37 °C for 1 h, supernatant was collected through centrifugation at 3000 rpm. The absorbance of the supernatant at 540 nm was measured using a microplate reader ($n = 3$).

The diluted red blood cell suspensions were added to saline and deionized water and served as negative and positive controls, respectively. The hemolysis ratio was calculated using the equation:

$$\text{Hemolysis ratio } (\%) = [(A_s - A_n)/(A_p - A_n)] \times 100\%$$

where A_s , A_n , and A_p represent the absorbance of the supernatant of the experimental group, negative control group, and positive control group, respectively.

2.6. Erythrocyte and platelet adhesion assays

Interfacial interactions between erythrocytes, platelets, and nanofiber membranes were assessed. Electrospun membranes were punched into 14 mm discs and incubated in PBS at 37 °C for 1 h. Platelet-rich plasma (PRP) was obtained by centrifuging whole blood at 3000 rpm for 10 min. One mL of PRP was dropped onto the surface of nanofiber membranes and placed at 37 °C for 1 h. Membranes were washed with PBS to remove unadhered erythrocytes or platelets and fixed with 2.5 % glutaraldehyde for 2 h. Finally dehydrated with graded ethanol and observed by SEM. PT and APTT assays were performed to assess the coagulation activation pathway of the prepared membranes. Citrate whole blood (9:1 whole blood and 3.8 % sodium citrate) was centrifuged at 3000 rpm for 15 min to obtain platelet-poor plasma (PPP). Various equal masses of nanofiber membranes were mixed with 100 μ L of PPP. Clotting times were determined using the PT kit and the APTT kit (Ellagic acid, Shanghai Sun Biotech Co., LTD), respectively, following the manufacturer's instructions ($n = 4$).

2.7. Antibacterial activity

Antibacterial activity of electrospun membranes was evaluated against commonly used bacteria: Gram-negative bacteria *Escherichia coli* (*E. coli*, ATCC 25922) and Gram-positive bacteria *Staphylococcus aureus* (*S. aureus*, ATCC 25923) and *Staphylococcus epidermidis* (*S. epidermidis*, ATCC 12228). Electrospun membranes were disinfected with 70 % ethanol for 1 h and then irradiated under UV (12 h for each side) prior to the introduction of bacteria. Bacteria were cultivated in broth (Mueller-Hinton) in a 37 °C shaker for 12 h. Add 100 μ L of germy inoculum (10^5 CFU/mL) dropwise to the surface of each sample and incubate at 37 °C for 24 h. The bacterial culture membranes were transferred to sterile PBS with agitation for 15 min, then diluted to the desired concentration (10^3 CFU/mL) and spread evenly on Luria-Bertani agar plates (Hopebio; HB0129). The colonies were counted after incubation at 37 °C for 24 h. Tissue culture plate (TCP) polystyrene was used as a control group.

2.8. Assessment of diabetic wound healing

According to our previous study [31], the diabetic rat model (blood glucose > 14 mmol/L) was created by administering a single dose of STZ to Sprague Dawley (SD) rats (~180 g, Shanghai JSJ Lab Animal Center) for 10 consecutive days. Electrospun membranes were punched into 10 mm discs and sterilized by UV irradiation prior to animal studies. Surgery was performed under sterile conditions. Diabetic rats were anesthetized by intraperitoneal injection of 2 % pentobarbital sodium (0.2 mL/100 g). Symmetrical circular full-thickness wounds were created (10 mm in diameter) on the back using a scalpel. Six wounds were made along the midline on the back of each rat. The wounds were then treated with different dressings: commercial bandages (3 M Adhesive Bandages), PCL/gelatin, MgAC-0.5, and MgAC-1 membranes. The wounds covered with commercial bandages served as a control. For each endpoint, four rats were used per group. Fifty-four rats were used for the study. To assess the wound healing process, the wound was observed and photographed at regular intervals. The area of unhealed wounds was measured by using Image J ($n = 4$ wounds per group) and wound healing curves were plotted.

Animals were sacrificed for analysis 7, 10, 14, and 21 days after surgery. Each wound area is excised from the skin. Tissues of wounds from each group were randomly taken and stored in liquid nitrogen for quantitative real-time polymerase chain reaction (qRT-PCR) ($n = 9$ wounds per group), and the remaining tissues were fixed with 4 % paraformaldehyde, embedded in paraffin, and sectioned into serial slides for histological and immunofluorescence staining. Detailed methods are provided in *Supplementary Information*.

2.9. Statistical analysis

Data were expressed as means \pm standard deviations. All data were

analyzed by one-way ANOVA with Tukey's *post hoc* tests. Statistical significance was considered at $p < 0.05$.

3. Results

3.1. Properties of electrospun membranes

We used TFE with 0.2 % acetic acid to solubilize PCL and gelatin as a control, as previous reports indicated that this formulation increased the miscibility between PCL and gelatin, resulting in smooth nanofiber morphology and improved mechanical strength of electrospun membranes [33,34]. In this study, we added an excess of acetic acid to ensure

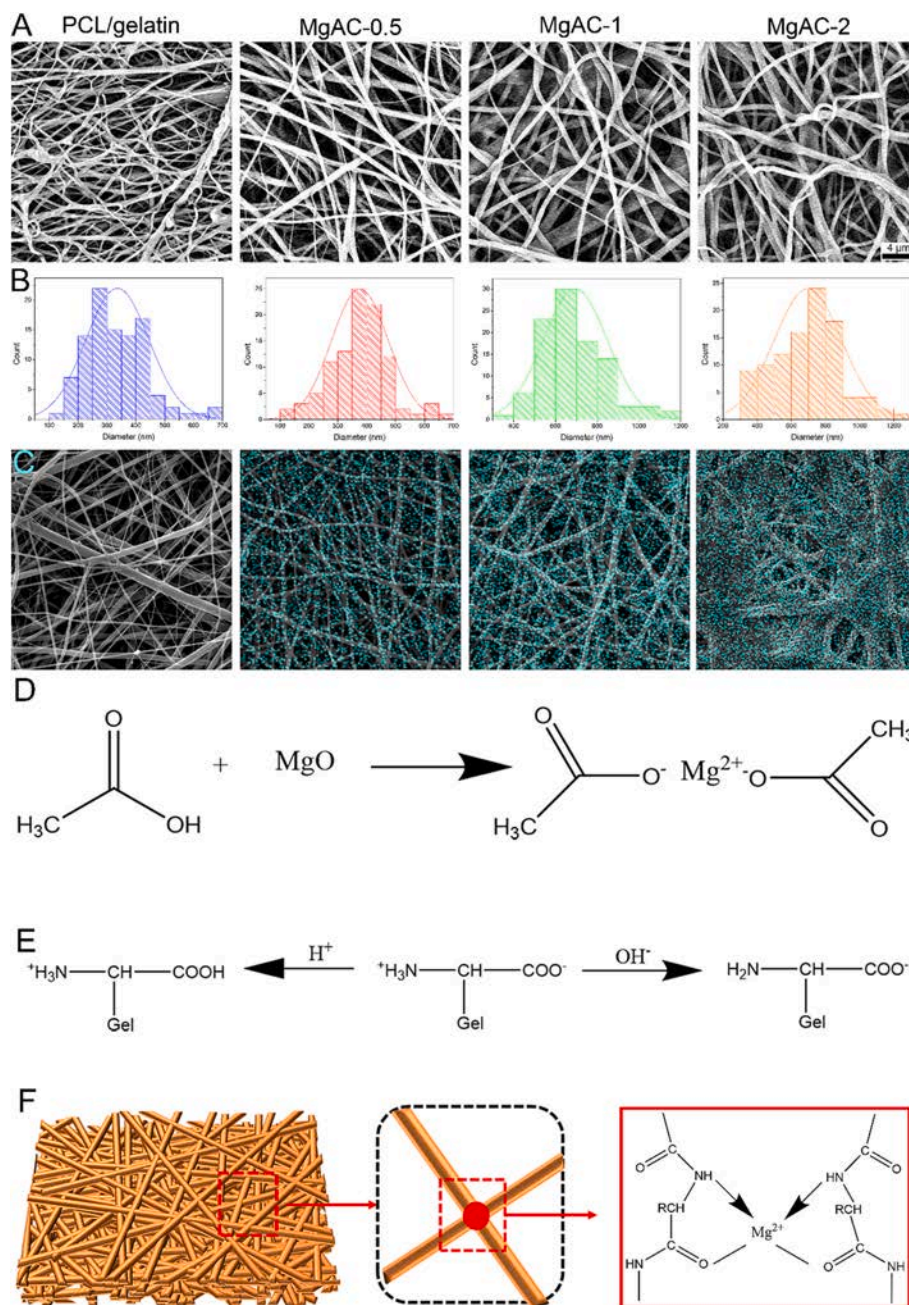


Fig. 1. Nanofiber structure and elemental analysis of electrospun membranes. SEM image shows that the electrospun membrane has a similar dense fibrous structure (A). The diameter distribution plot (B) shows that fiber diameter increases with increasing MgAC content in the electrospinning solution. The elemental plot shows that the density of magnesium (C) within the electrospun membrane increases with the amount of incorporated MgAC. Chemical reaction equation between acetic acid and magnesium oxide (D). Charge phenomena of gelatin at different pH values (E). A schematic of the formation of a chelate complex between gelatin and Mg^{2+} (F).

complete reaction with MgO nanoparticles and generate MgAC, which showed profound effects on the subsequent electrospinning process (Fig. 1D). Acetic acid is a weak acid that is incompletely ionized in TFE solution. The addition of MgO nanoparticles to PCL/gelatin led to a

rapid reaction between MgO and acetic acid, accelerating the ionization of acetic acid, which in turn promoted the reaction between MgO nanoparticles and acetic acid. Gelatin is a widely available and inexpensive degradable biomaterial for natural proteins. Both =O and —NH

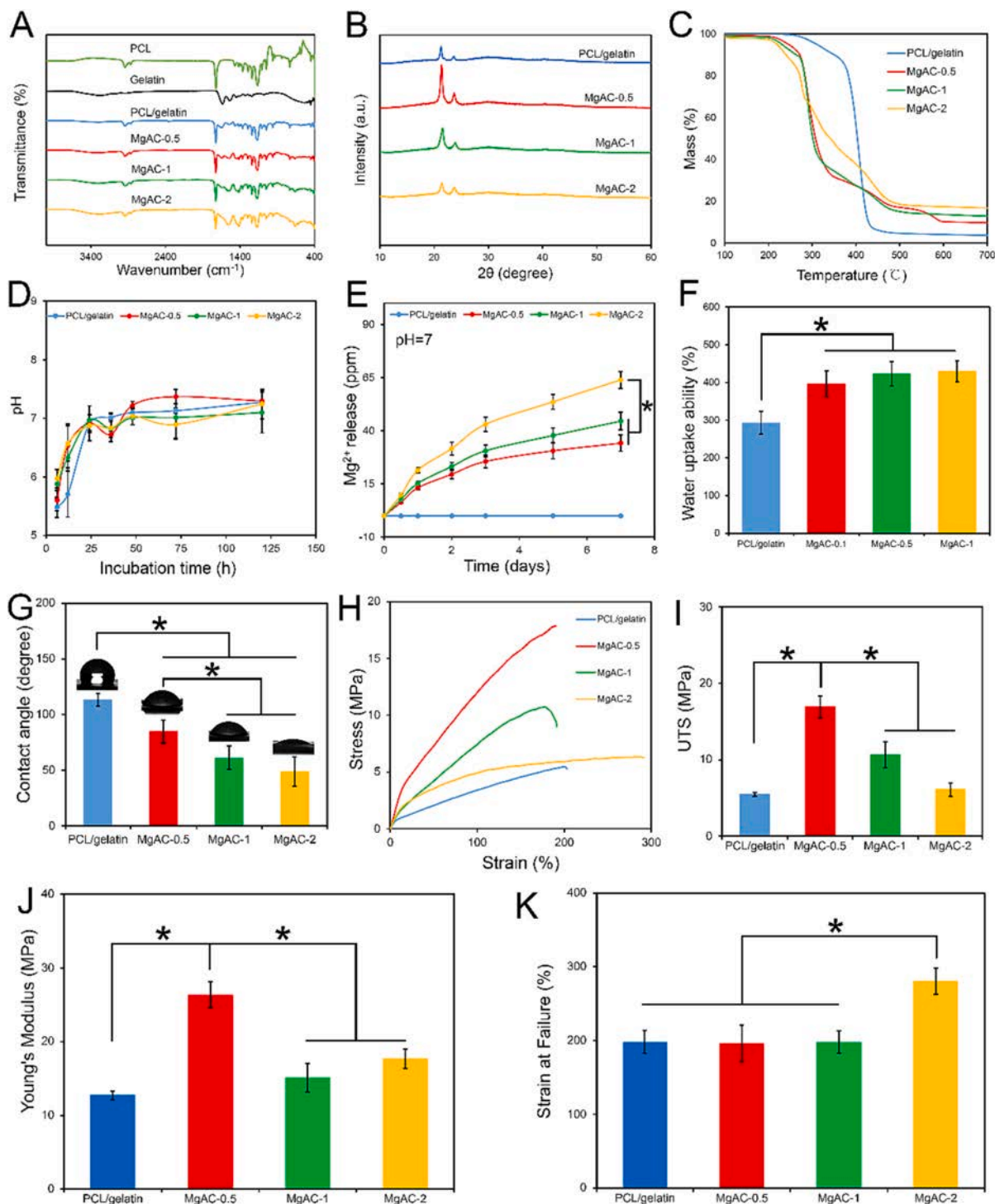


Fig. 2. Physicochemical properties of electrospun membranes. FTIR spectra show that MgAC have a typical peak at 660 cm^{-1} , which could be found in the MgAC-containing nanofiber membranes (A). Similarly, the XRD pattern shows two major diffraction peaks of PCL at $2\theta = 21.40^\circ$ and 23.79° (B). TGA analysis showed that the membranes containing MgAC had lower initial degradation temperatures than the PCL/gelatin membranes, indicating that the addition of MgAC reduced the thermal stability of the membrane (C). The pH of the PCL/gelatin/MgAC nanofiber membrane changed from acidic to neutral (D). Cumulative magnesium ion release (E) of membrane incubations. The water absorption capacity (F) of PCL/gelatin/MgAC electrospun membranes was higher than that of PCL/gelatin electrospun membranes. The contact angle (G) of nanofiber membrane decreases gradually with the increase of MgAC content. Tensile mechanical properties of nanofiber membranes in the wet state. The MgAC-0.5 membrane shows a higher stress-strain curve (H) with greater UTS (I) and Young's modulus (J) and comparable breaking strain (K) compared with the PCL/gelatin membrane. One-way ANOVA with Tukey's *post hoc* test, $n = 3-4$, * indicates $p < 0.05$.

groups carrying lone electron pairs on the amide bond in gelatin molecules provided lone electron pairs to form coordination bonds for Mg^{2+} (Fig. 1E). Therefore, chemical cross-linking between nanofibers can be achieved through the formation of chelate complexes between magnesium ions and gelatin (Fig. 1F).

SEM images revealed the dense nanofiber structure of electrospun membranes consisting of continuous and smooth nanofibers (Fig. 1A). In general, PCL/gelatin/MgAC membranes had relatively uniform fiber diameter (Fig. 1B) and relatively smooth surfaces compared to the PCL/gelatin membrane. EDS images showed the absence of Mg within the PCL/gelatin membrane, whereas Mg was uniformly distributed in the MgAC-incorporated membranes (Fig. 1C). The elemental density of magnesium increased proportionally from MgAC-0.5 to MgAC-2 membranes.

FTIR spectra of electrospun membranes are shown in Fig. 2A. The peak at 660 cm^{-1} belonged to the characteristic peak of magnesium acetate. The amide I, II, and III bands of gelatin in PCL/gelatin membranes were at 1723 cm^{-1} , 1647 cm^{-1} , and 1365 cm^{-1} , respectively. In the infrared spectrum of MgAC-incorporated membranes, the amide II band sharply decreased, indicating that the influence of magnesium acetate on the amide group was in the amide II band, which is a coupling peak generated by the N—H in-plane bending vibration and the C—H stretching vibration. It can be speculated that this is due to the coordination between the amide groups of gelatin and the ions of magnesium acetate, which inhibits the normal vibration of the amide group [36]. Fig. 2B shows the XRD pattern. Electrospun membranes showed two main diffraction peaks of PCL at $2\theta = 21.40^\circ$ and 23.79° . There is no diffraction peak in MgAC, which indicates that MgAC exists in the nanofiber membranes in an amorphous form. The thermal stability of electrospun membranes was assessed by TGA (Fig. 2C). The PCL/gelatin membrane had an initial degradation temperature that was much higher than all MgAC-incorporated electrospun membranes. These results indicate that the incorporation of MgAC into PCL/gelatin decreases the thermal stability.

When incubated in saline at 37°C , the pH of solutions with electrospun membranes was 5–6, probably due to residual acetic acid (Fig. 2D). It became neutral after 24 h. Continued release of Mg^{2+} from electrospun membranes was observed throughout the incubation process (Fig. 2E). Generally, Mg^{2+} was slowly released from electrospun membranes. However, the rate of Mg^{2+} release was pH-dependent. Mg^{2+} showed a relatively slower release rate in an acidic environment at pH 5 compared with the release rate in an alkaline environment at pH 8 (Fig. S1). Under alkaline conditions, sodium hydroxide (NaOH) breaks the equilibrium of Mg^{2+} chelated with gelatin, and NaOH reacts with MgAC to form magnesium hydroxide precipitate. It leads to faster degradation of MgAC-incorporated membranes under alkaline conditions than under acidic conditions (Fig. S2). The presence of magnesium acetate significantly improved the water absorption capacity (Fig. 2F) and wettability (Fig. 2G) of electrospun membranes. The contact angles of electrospun membranes gradually decreased with the increase of MgAC content. These results suggest that the presence of MgAC makes the electrospun membranes more hydrophilic.

Wound dressings readily absorb wound exudate, therefore we evaluated tensile properties of electrospun membranes in the wet state. Electrospun membranes showed typical curves with different tensile strengths and strains at break in the wet state (Fig. 2H). The presence of MgAC improved the tensile strengths of electrospun membranes. Specifically, the MgAC-0.5 membrane had a UTS of $16.9 \pm 0.1\text{ MPa}$, which was significantly higher than that of the PCL/gelatin ($5.5 \pm 0.3\text{ MPa}$), MgAC-1 ($10.7 \pm 1.7\text{ MPa}$), and MgAC-2 membranes ($6.1 \pm 0.9\text{ MPa}$) (Fig. 2I). The tensile moduli of electrospun membranes showed a similar trend in response to the incorporated MgAC, specifically, it first increased and then decreased with the increasing amount of MgAC (Fig. 2J). The tensile modulus of MgAC-0.5 is $26.3 \pm 1.7\text{ MPa}$, which is significantly higher than other electrospun membranes. The breaking strains of electrospun membranes (Fig. 2K) were not so profoundly

affected by incorporated MgAC. One exception was that the MgAC-2 membrane had a significantly higher breaking strain than the other membranes.

3.2. Cytocompatibility of electrospun membranes

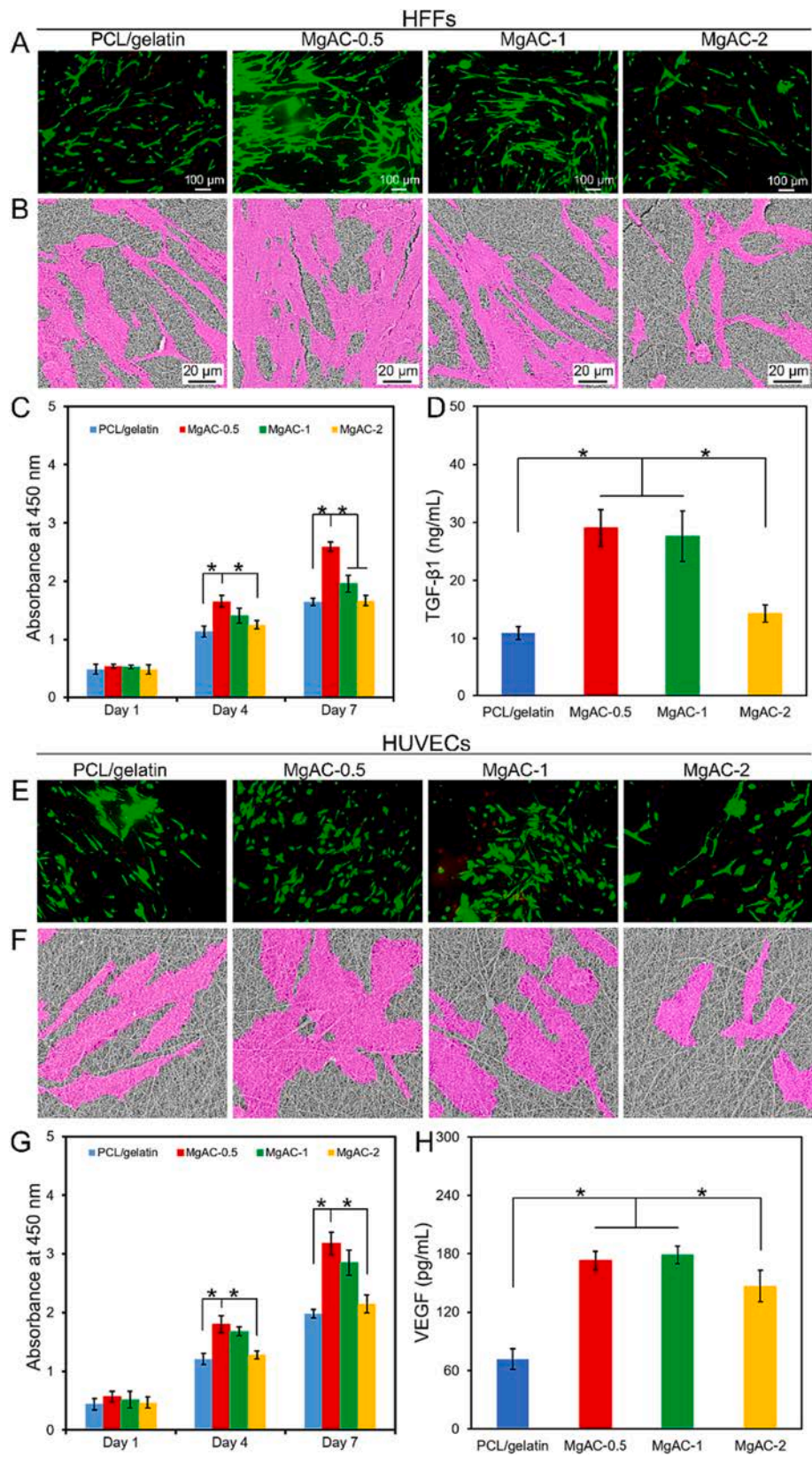
Fibroblasts are not only a commonly used cell line for evaluating cytocompatibility but also the master cells for extracellular matrix production during wound healing. As shown by live/dead staining (Fig. 3A) and SEM images (Fig. 3B), HFFs adhered well to electrospun membranes and exhibited a spindle shape. Compared to the PCL/gelatin, MgAC-1, and MgAC-2 membranes, HFFs showed more viable cells (Fig. 3A, green staining) and greater coverage (Fig. 3B) on the MgAC-0.5 membrane. This is consistent with significantly higher proliferation rates of HFF cells on the MgAC-0.5 membrane as determined by the CCK-8 assay (Fig. 3C) ($p < 0.05$). In addition, the MgAC-0.5 membrane promoted pro-healing growth factor TGF- β 1 secretion which was three-fold as high as the PCL/gelatin membrane (Fig. 3D).

Similarly, HUVECs exhibited higher activity on membranes incorporated with MgAC (Fig. 3E). SEM images indicate that HUVECs showed the greatest coverage on the MgAC-0.5 membrane (Fig. 3F). Cytokine production by HUVECs activated by membranes incorporating MgAC was dose-dependent (Fig. 3G). Both MgAC-0.5 and MgAC membranes promoted VEGF production, while MgAC-2 membranes significantly inhibited VEGF expression in comparison to MgAC-0.5 and MgAC membranes (Fig. 3H).

3.3. Blood coagulation and hemocompatibility performance

A dynamic whole blood clotting model was used to assess the *in vitro* hemostatic behaviors (Fig. 4A). There were more blood clots on the surface electrospun membranes than the gauze. The gauze control group showed a clear rise in red color after rinsing with water, indicating a lower blood clotting capacity of the gauze. For the PCL/gelatin membrane, most of the blood was coagulated, leaving reddish-flushing water. Instead, the blood was completely coagulated on the MgAC-0.5 membrane, and the supernatant was clear and transparent. With increasing levels of MgAC, the red color of electrospun membranes and supernatants gradually deepened. This is likely because higher MgAC causes cell membrane disintegration. The absorbance value of the hemoglobin solution produced by uncoagulated red blood cells was used to compute the coagulation index (BCI) [37]. The higher the absorbance value of the hemoglobin solution, the slower the clotting rate. The highest BCI value ($87.7 \pm 4.5\%$) was found for the MgAC-2 membrane group, indicating its slowest clotting rate (Fig. 4B). In addition, the BCI value of MgAC-0.5 membrane ($21.9 \pm 4.4\%$) was lower than that of other membranes ($43.2 \pm 3.3\%$) and commercial agents ($23.7 \pm 4.6\%$), suggesting its greatest coagulation ability. Blood clotting time measurements were used to assess hemostatic characteristics. After adding blood for a certain time, all samples were capable of producing blood clots (Fig. 4C). The coagulation rate of the MgAC-0.5 nanofiber membrane ($136 \pm 4\text{ s}$) was significantly faster than other membranes and the gauze (Fig. 4D). The hemocompatibility was evaluated using an *in vitro* hemolysis test as previously reported [35]. Fig. 4E shows the macroscopic hue of the supernatants of electrospun membranes. The rate of hemolysis increased as the amounts of MgAC increased (Fig. 4F). Both the PCL/gelatin and MgAC-0.5 membranes showed hemolysis rates of $< 5\%$, but the MgAC-1 and MgAC-2 membranes had hemolysis rates of $10\%–30\%$.

Fig. 5 depicts the surface adherence and morphologies of erythrocytes and platelets on the nanofibers. A small number of erythrocytes and platelets were observed adhering to the PCL/gelatin membrane, whereas the number of aggregated erythrocytes and platelets was significantly higher on the MgAC-incorporated membranes. Activated partial thromboplastin time (APTT) (Fig. 5C) and prothrombin time (PT) (Fig. 5D) assays were used to calculate the effects of various substances on the intrinsic and extrinsic coagulation pathways, respectively [38].



(caption on next page)

Fig. 3. Cytocompatibility and bioactivity of electrospun membranes *in vitro*. Live/dead assay revealed that the HFFs are of spindle-shape and exhibit higher viability on the MgAC-0.5 membrane (A). The HFFs are attached and spread well on the MgAC-0.5 membrane, and the cell area is larger as shown in the SEM images (B). Similarly, live/dead staining (E) shows that the HUVECs are predominantly viable (green) on MgAC-0.5 membranes. On the other hand, MgAC-1 and MgAC-2 membranes exhibit greater proportion of dead cells (red). SEM images (F) show that the HUVECs are well-spread with large cell area on MgAC-0.5 membranes than that of the MgAC-1 and MgAC-2 membranes. CCK-8 assay of HUVECs (C) and HFFs (G) shows that the MgAC-0.5 membrane supports significantly higher cell proliferation rate compared to the other membranes, which further corresponded to the highest TGF- β 1(D) secretion and VEGF production (H) in these membranes than the other membranes. One-way ANOVA with Tukey's *post hoc* test, $n = 4$, * indicates $p < 0.05$. (For interpretation of the references to color in this figure legend, the reader is referred to the web version of this article.)

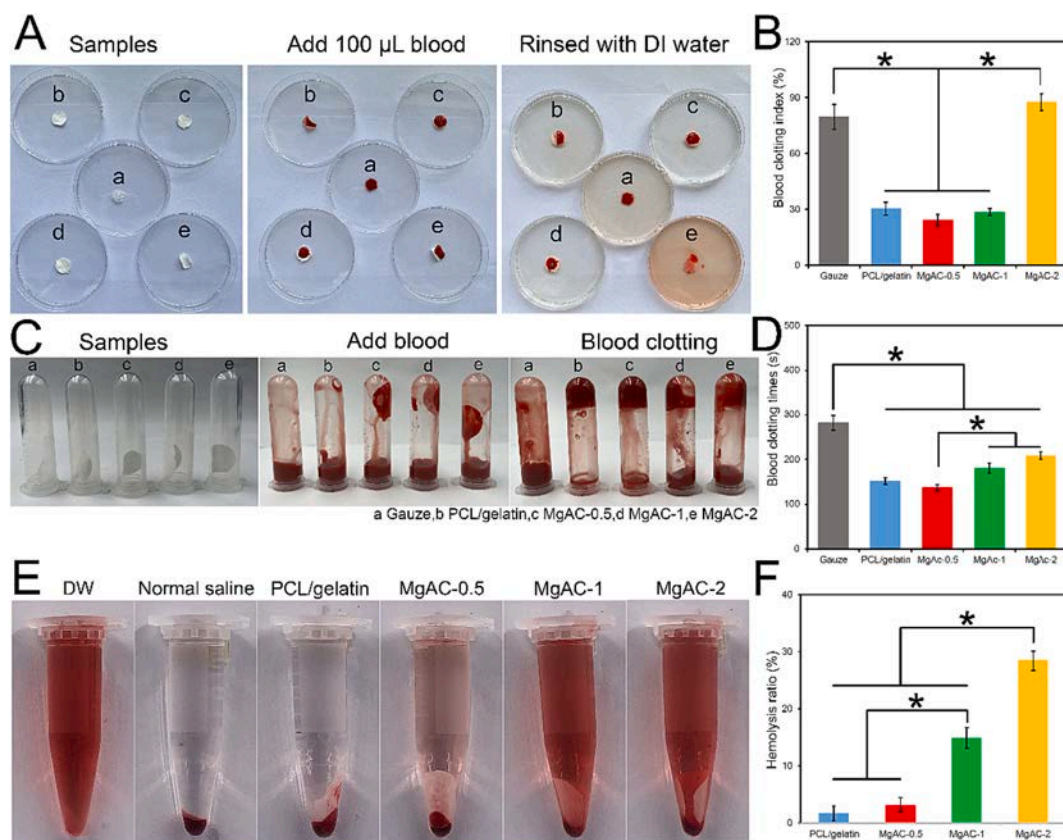


Fig. 4. *In vitro* hemostatic capacity and hemocompatibility evaluation. (A) A dynamic whole-blood clotting model is employed to evaluate the *in vitro* hemostatic property. (B) The corresponding BCI values of electrospun membranes. (C) Photographs of blood clotting formation process. (D) The *in vitro* hemostatic properties of MgAC-incorporated membranes are evaluated by measuring the blood clotting time. (E) Photographs from hemolytic activity assay of the MgAC-incorporated membranes using normal saline as negative control and water as the positive control. (F) The hemolysis ratio of MgAC-incorporated membranes. One-way ANOVA with Tukey's *post hoc* test, $n = 4$, * indicates $p < 0.05$.

The MgAC-incorporated membranes had lower ATPP values than the PCL/gelatin membrane. However, there was no significant difference in PT values among these membranes. The results indicate that MgAC-incorporated membranes could activate the intrinsic coagulation pathway.

3.4. *In vitro* antibacterial activity

The antibacterial activity of MgAC-incorporated membranes against *E. coli*, *S. aureus*, and *S. epidermidis* was tested. Fig. 6A-C shows bacterial colonies after co-culture with MgAC-incorporated membranes. Compared to the TCP control, the PCL/gelatin membrane had comparable bacterial colonies, indicating that it does not have antibacterial activity. MgAC-incorporated membranes showed much fewer bacterial colonies, indicating that they had some antibacterial activity against *E. coli* (Fig. 6D), *S. aureus* (Fig. 6E), and *S. epidermidis* (Fig. 6F), albeit with different efficiencies. Although MgAC-incorporated membranes did not kill all bacteria, the number of bacteria incorporated on the MgAC membrane was much lower relative to the PCL/gelatin

membrane. In addition, the number of colonies corresponding to the different strains of bacteria in each sample was calculated, with the same trend as the inhibition rate (Fig. S3).

3.5. Diabetic wound healing and gene expression

Full-thickness skin wounds with a diameter of 10 mm were excised in diabetic rats to evaluate the effect of electrospun membranes on diabetic wound healing. Wound healing was observed at 7, 10, 14, and 21 days after surgery (Fig. 7A). Wounds of the control, PCL/gelatin membrane, and MgAC-1 membrane groups developed the common complications of wound infection of chronic diabetic wounds at day 7, which decreased to about 60 % of their original size by day 21 (Fig. 7B). In contrast, closure rate was significantly accelerated for the MgAC-0.5 membrane-treated wound, which reduced to 20 % of its original size by day 21.

Expression levels of the pro-inflammatory genes IL-1 β and TNF- α and the pro-healing genes TGF- β 1 and α -SMA were determined by qRT-PCR 10 days after surgery (Fig. 7C-F). The expression levels of pro-healing genes in the wounds of the PCL/gelatin membrane group were

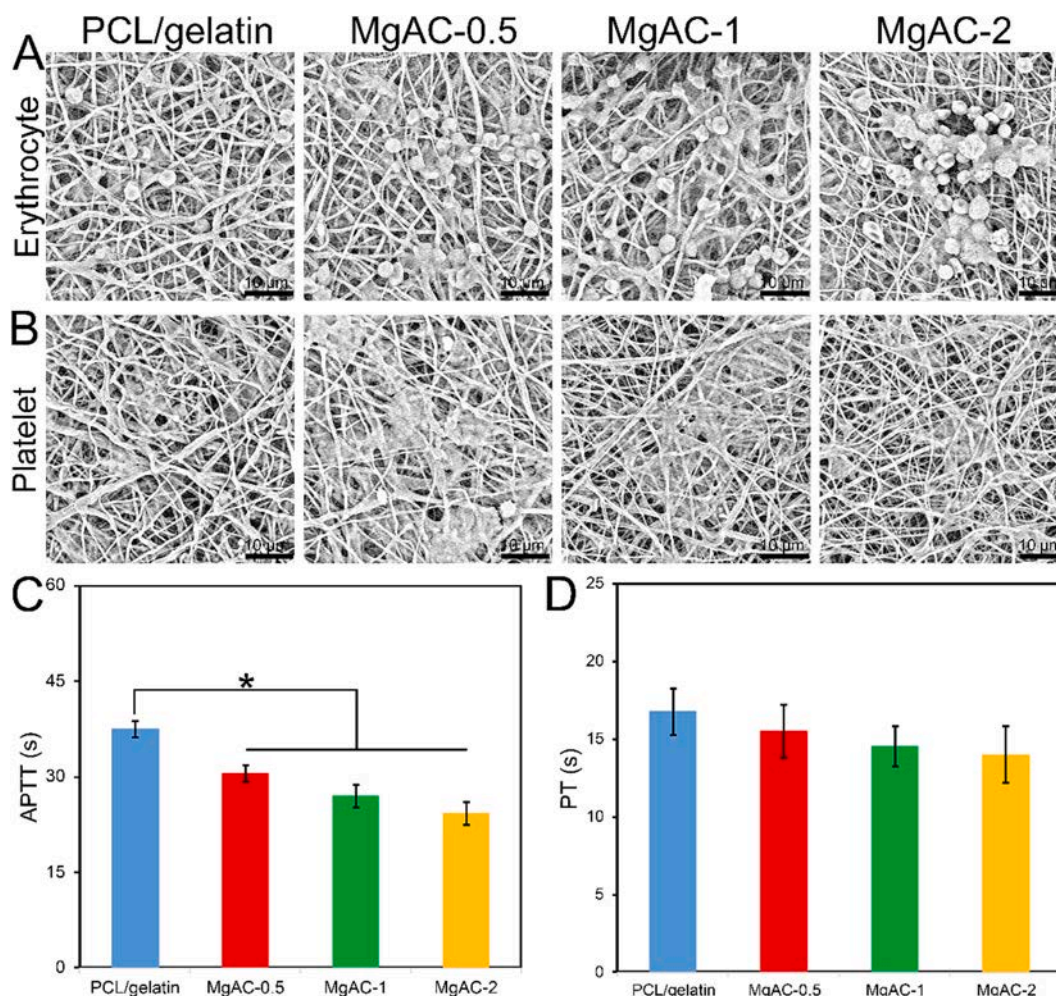


Fig. 5. *In vitro* hemocompatibility evaluation. SEM images of red blood cells (A) and platelets (B) adhered to the surface of electrospun membrane. PT (C) and APTT (D) values. One-way ANOVA with Tukey's *post hoc* test, $n = 4$, * indicates $p < 0.05$. (For interpretation of the references to color in this figure legend, the reader is referred to the web version of this article.)

comparable to those in the control group ($p > 0.05$), but the expression levels of pro-inflammatory genes were slightly higher than those in the control group. In contrast, MgAC-incorporated membranes significantly up-regulated the expression levels of the pro-healing genes TGF- β 1 and α -SMA ($p < 0.05$) and down-regulated the expression level of the pro-inflammatory genes IL-1 β and TNF- α compared with the PCL/gelatin membrane and control groups ($p < 0.05$). These results demonstrate that the MgAC-incorporated membranes accelerate the closure rate of diabetic wounds by modulating inflammation.

3.6. Histological assessments of healing wounds

Structural and functional regeneration of diabetic full-thickness wounds was examined by histological staining (Fig. 8). H&E-stained images showing full-thickness wound infection in diabetic rats (Fig. 8A). H&E images show that the MgAC-0.5 membrane-treated wound had no evident biofilm formation on the wound beds. However, wounds of other groups showed moderate to severe inflammation with different degrees of infection as revealed by biofilm formation and inflammatory cell accumulation underneath the dense purple bacterial layer. At day 21, MgAC-0.5 membrane-treated wounds closed with moderate epidermal hyperplasia, with epithelialization overlying granulation tissue. Regenerated tissue showed mature epidermis and hair follicles. In contrast, wounds of other groups did not heal at day 21. Furthermore, Masson's trichrome staining (Fig. 8B) showed that wounds treated with

MgAC-0.5 membranes had more mature collagen fiber bundles, indicating good wound healing.

3.7. Immunofluorescence staining of healing wounds

Immunofluorescence staining was used to assess inflammation, angiogenesis, and functional recovery in the full-thickness wound skin of diabetic rats (Fig. 9). Compared with other groups, CD31-positive cells of the MgAC-0.5 membrane-treated wound were densely distributed in the regenerated skin tissue, while these cells were sparsely present in the granulation tissue of the control and PCL/gelatin groups. Similarly, CD68-positive cells were weakly expressed in the MgO-0.5 membrane-treated wound relative to the control and PCL/gelatin groups (Fig. 9A). CD86/CD206 staining was used to mark macrophage differentiation. At day 10, M2 macrophages were predominantly present in the adjacent tissue around the wound in diabetic rats (Fig. 9B). A significant increase in the M2 macrophage subset was found in the regenerated skin of the MgAC-0.5 group, suggesting its promotive role in tissue regeneration.

Full-thickness wound epithelialization in diabetic rats on days 14 and 21 was assessed by K10 (epidermal differentiation marker)/K14 (epidermal basal cell marker) staining (Fig. 9C). At day 14, the MgAC-0.5 membrane-treated wound had already started to epithelialize, while the other groups did not. MgAC-0.5 membrane-treated wounds showed mature epidermis on day 21 (Fig. 9D). In contrast, wounds in the

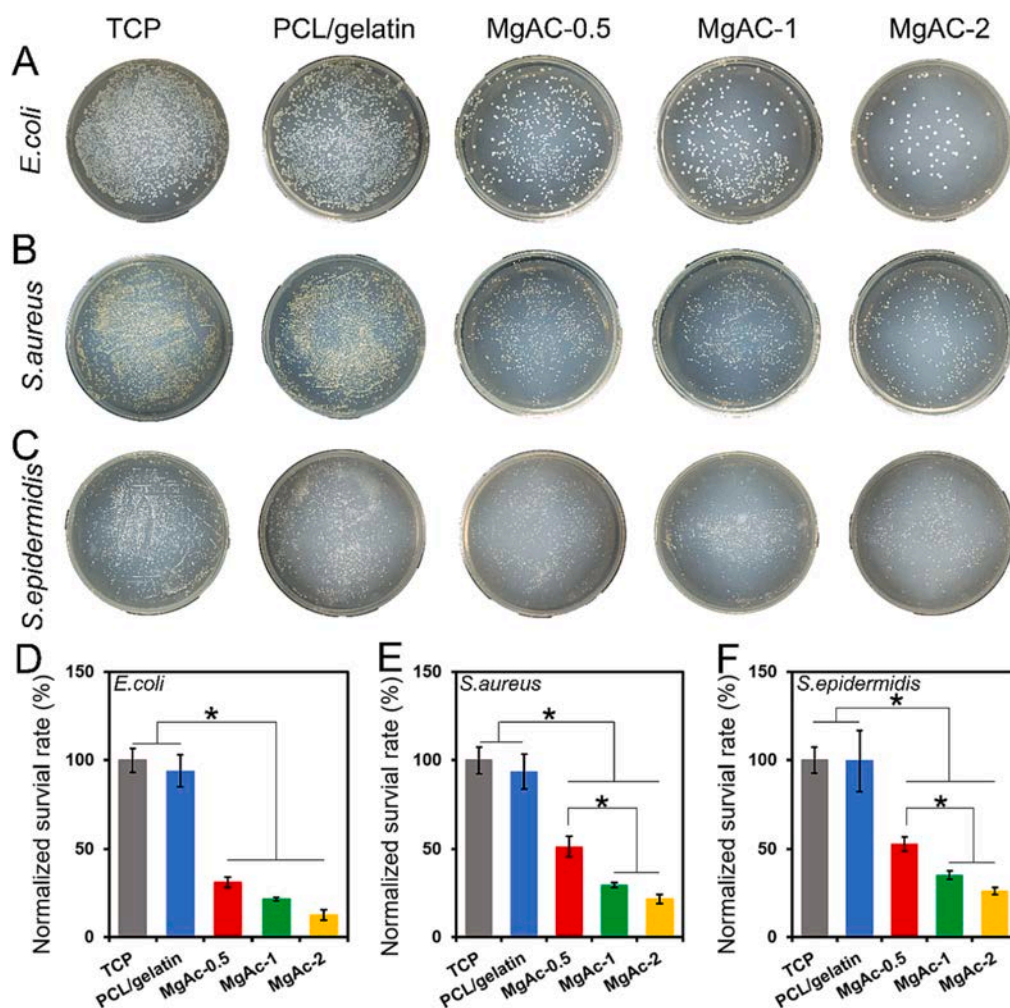


Fig. 6. *In vitro* antibacterial properties of MgAC-incorporated membranes. Macroscopic images show *E. coli* (A), *S. aureus* (B), and *S. epidermidis* (C) colonies grown on broth agar plates after treating with PCL/gelatin/MgAC nanofiber membranes. Quantitatively, MgAC-incorporated membranes significantly inhibit bacterial growth with respect to the PCL/gelatin membrane and TCP control in a dose-dependent manner. Obviously, MgAC-incorporated membranes are more powerful in inhibiting the growth of *E. coli* (D) when compared with their inhibitory effects on *S. aureus* (E) and *S. epidermidis* (F). One-way ANOVA with Tukey's *post hoc* test, $n = 4$, * indicates $p < 0.05$.

control group, PCL/gelatin group, and MgAC-1 showed partial coverage of K10-positive epidermis and a weaker basal layer of K14 epidermis, suggesting the immature state of regenerating epidermis.

4. Discussion

In our previous studies, we have demonstrated that the incorporation of MgO nanoparticles into electrospun membranes improves the physicochemical properties and bioactivity of electrospun membranes. Despite this, we observed limitations associated with incorporated MgO nanoparticles: burst release of magnesium ions and significantly elevated pH of the surrounding local environment due to MgO hydrolysis. To overcome these problems, we sought to replace MgO nanoparticles with magnesium chloride or magnesium acetate particles for electrospinning but failed for several reasons. Herein we reported an effort of converting MgO into magnesium acetate during the preparation of electrospun solution and demonstrated that it could solve these problems. Our results show that MgO nanoparticles completely transformed into MgAC in the electrospun solution by adding excess acetic acid. The absence of particles and the uniform distribution of elemental magnesium in the SEM image (Fig. 1) indicate that magnesium oxide has completely reacted to form MgAC, uniformly incorporated within the electrospun membrane.

The tensile mechanical properties of MgAC-incorporated membranes were found to be much higher than the PCL/gelatin membranes (Fig. 2H). Interestingly, the MgAC-0.5 membrane had the highest tensile mechanical strength, while the MgAC-2 membrane showed good flexibility with a larger fracture strain (Fig. 2J). We speculate that the reason for this phenomenon is related to the presence of MgAC. It is reported that Mg^{2+} can form chelate rings with carboxyl and amino groups ligated on the surface of gelatin [36]. FTIR spectra show a significant reduction in amide II band owing to the formation of coordination bonds between the amide group in gelatin and Mg^{2+} in magnesium acetate, and the nucleation of magnesium acetate at this site inhibits the normal vibrations of the amide group (Fig. 2A). Similarly, XRD spectra reveal the absence of sharp diffraction peak of MgO ($2\theta = 42.82^\circ$) [34], which also proves that the MgO nanoparticles have been completely converted to MgAC and are present in the nanofiber membranes in ionic form (Fig. 2B), confirming the formation of chelates between gelatin and Mg^{2+} in the nanofibers. This allows the formation of chemical crosslinks within and between the nanofibers thus enhancing the mechanical properties of the nanofiber membrane (Fig. 1I). However, MgAC-1 and MgAC-2 membranes had lower UTS in comparison to the MgAC-0.5 membrane, indicating that increased amount of MgAC within the nanofibers could disrupt chelate rings.

The conversion of MgO into MgAC also gives other benefits. First, it

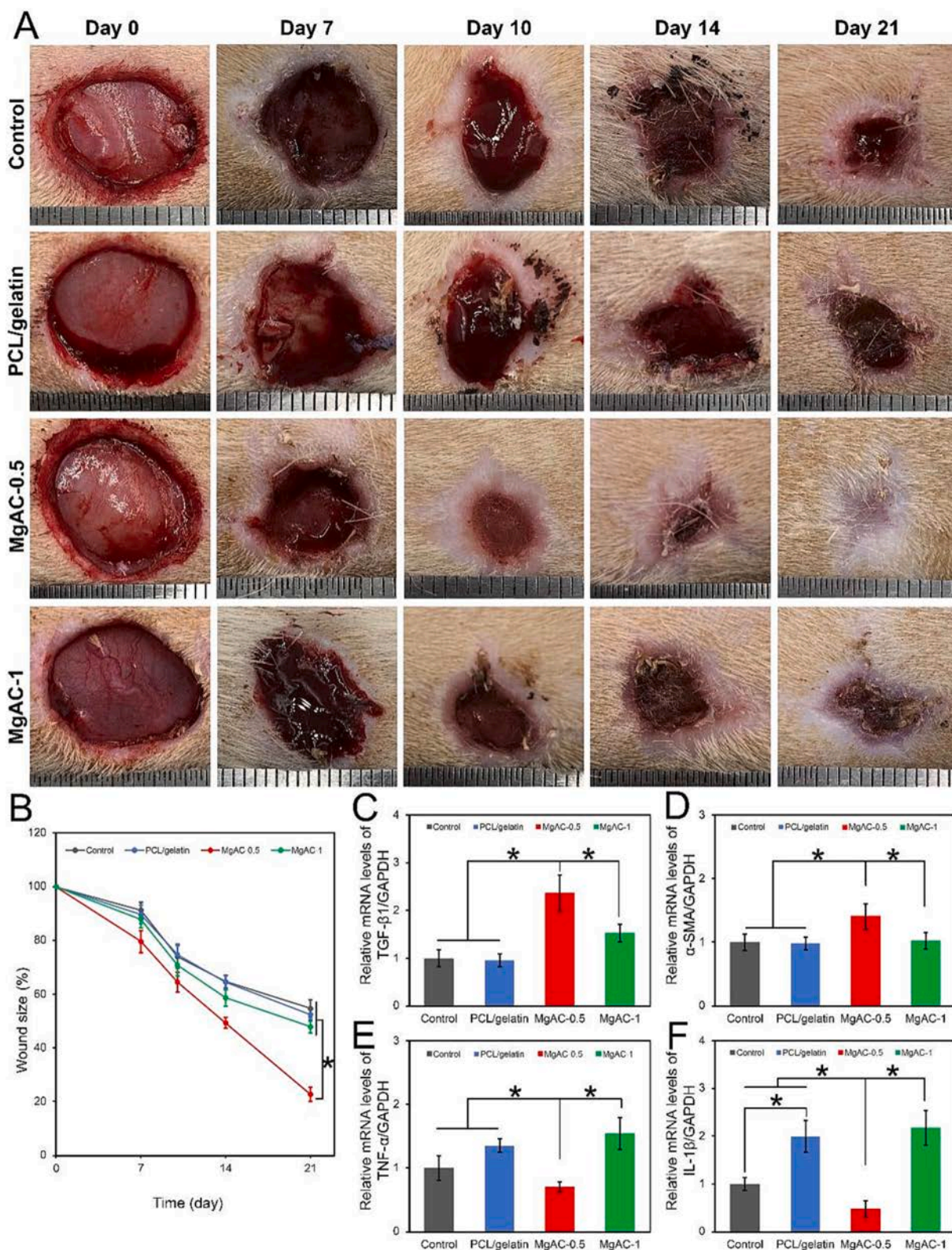


Fig. 7. Assessments of full-thickness defect wound healing in a STZ diabetic rat model. Gross appearance of diabetic wounds with MgAC-incorporated membranes treatments for 14 days (A). The MgAC-incorporated membrane effectively suppresses bacterial infection and reduces wound swelling. Wound closure curves (B) demonstrate that MgAC-incorporated membranes significantly accelerate the healing process of diabetic wounds compared with the PCL/gelatin membrane and control groups. Two-way ANOVA with Tukey's *post hoc* test, $n = 3$, * indicates $p < 0.05$. qRT-PCR analysis indicates that MgAC-incorporated membrane significantly downregulates the gene expression levels of TNF- α (E) and IL-1 β (F). Simultaneously, it significantly upregulates the pro-healing gene expression levels of TGF- β 1 (C) and α -SMA (D). Two-way ANOVA with Tukey's *post hoc* test, $n = 3$, * indicates $p < 0.05$.

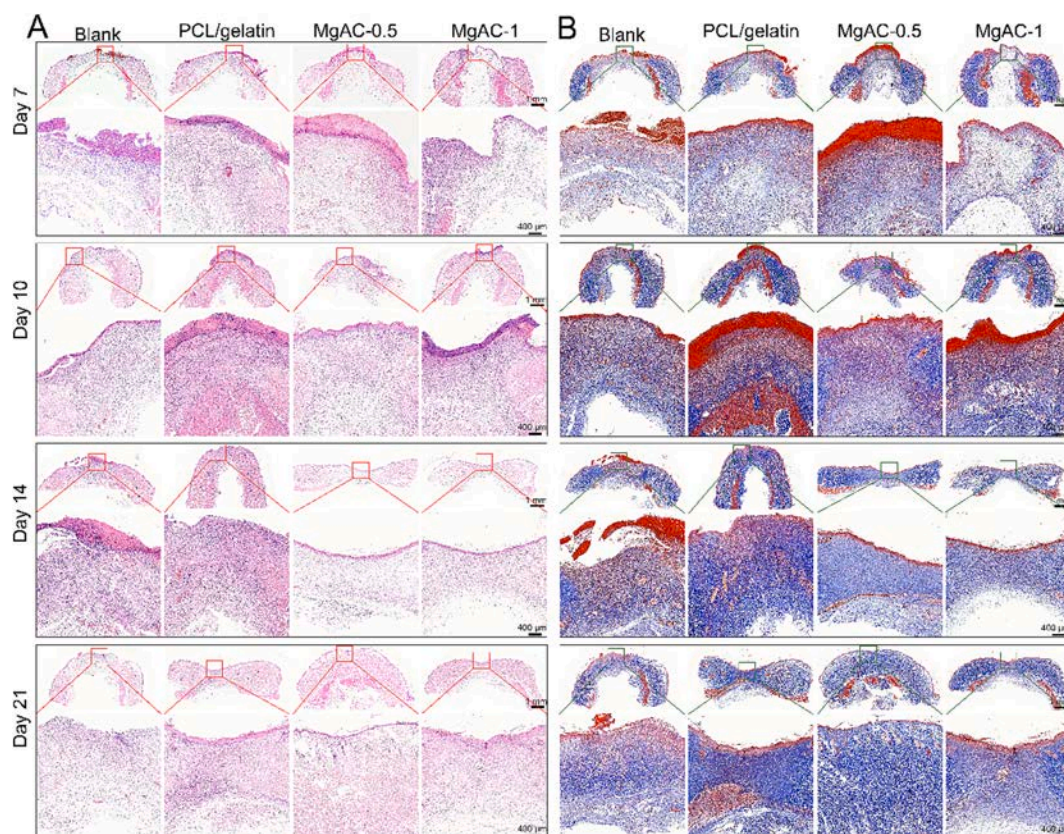


Fig. 8. Histological analyses of healing wounds at days 7, 10, 14 and 21 by H&E (A), Masson's Trichrome (B) staining. At day 3, all wounds show full-thickness defects without healing tissue. The MgAC-0.5 and MgAC-1 membrane-treated wounds show collagen deposition as revealed by Masson's Trichrome staining (B), while the other groups have scarce collagen deposition.

circumvents the MgO-hydrolysis caused increase of pH in local environment (Fig. 2D). This makes the MgAC-incorporated membranes safer for *in vivo* use. Secondly, it prolongs the Mg^{2+} release from nanofibers in comparison to MgO-incorporated nanofiber membranes. This is attributed to chelate rings between Mg^{2+} with carboxyl and amino groups ligated of gelatin. Prolonged and slower release of Mg^{2+} therefore might not only be beneficial for diabetic wound management but also for other biomedical applications. Lastly, the presence of MgAC makes electrospun membranes more hydrophilic (Fig. 2G) with strong water absorption capacity (Fig. 2F), making them more attractive for wound dressing application. However, the conversion of MgO into MgAC leads to lower antibacterial activity in both *in vivo* and *in vitro* studies (Figs. 6 and 7) compared with the MgO-incorporated membranes [34]. This result suggests that oxidize-related antibacterial capacity is likely the primary contribution of the antibacterial activity of the magnesium-based materials.

The first stage of wound healing is the hemostasis phase, which refers to the body first promoting the contraction of vascular smooth muscle cells through a neuroreflex mechanism, leading to the rapid contraction of damaged blood vessels and triggering hemostasis [39]. Then, platelets accumulate in the wound to form a clot and begin hemostasis [40], this requires dressing materials to have good hemostatic capacity. Gelatin and its blends with other biomaterials show excellent hemostasis capacity and have been widely used as hemostats [41]. Previously, our group had reported an electrospun sponge composed of gelatin and demonstrated that the amino group of gelatin can rapidly induce coagulation by promoting platelet aggregation [35]. Magnesium has been found to exhibit pro-coagulant activity *in vivo* and plays a role in regulating inflammatory factors [42,43]. Given these advantages, incorporating magnesium into gelatin-containing nanofiber membranes shows interest for this application. Our results show that gelatin and Mg^{2+} have

a synergic hemostatic effect, enabling MgAC-incorporated membranes with improved coagulation (Fig. 4) and hemostatic capacity *in vitro* (Fig. 5).

Diabetic wound is simultaneously a chronic, deep, infected, and ulcerated trauma, characterized by high levels of inflammatory cytokines, matrix metalloproteinases (MMPs) and reactive oxygen species (ROS), poor angiogenesis, and persistent infection [44–47]. A hallmark impact of these dysregulated expressions in diabetic wounds is the inhibited expression of pro-angiogenic factor VEGF and pro-healing factor TGF- β 1. Our data show that the MgAC-incorporated membranes are capable of promoting the expression of these factors both in *in vitro* (Fig. 3) and *in vivo* (Fig. 9) studies. In *in vitro* study, we observed that nanofiber membranes with low Mg^{2+} content significantly enhanced the proliferation of fibroblasts and HUVEC, while those with high Mg^{2+} content inhibited their growth (Fig. 3) in line with our previous reports [32–34,48,49]. Consequently, for treating wounds in diabetic rats, we selected MgAC-0.5 and MgAC-1 nanofiber membranes.

The improved wound healing observed for the MgAC-incorporated membrane-treated diabetic wound is attributable to the anti-inflammatory and pro-angiogenic effects of magnesium ions (Figs. 7 and 8). In the late phase of inflammation in normal trauma, macrophages change from pro-inflammatory M1 macrophages to repair-promoting M2 macrophages, accelerating the wound healing process. However, it is difficult for macrophages to transit from M1 to M2 in diabetic trauma, leading to the production of pigment epithelium-derived factors and inhibits angiogenesis [47]. Diabetic wounds are in a prolonged inflammatory phase, which continues to produce high expression of inflammatory cytokines and significantly reduced expression of growth factors such as transforming growth factor- β , hindering the proliferation and migration of keratin-forming cells and slowing down the process of re-epithelialization [50–52]. Our data

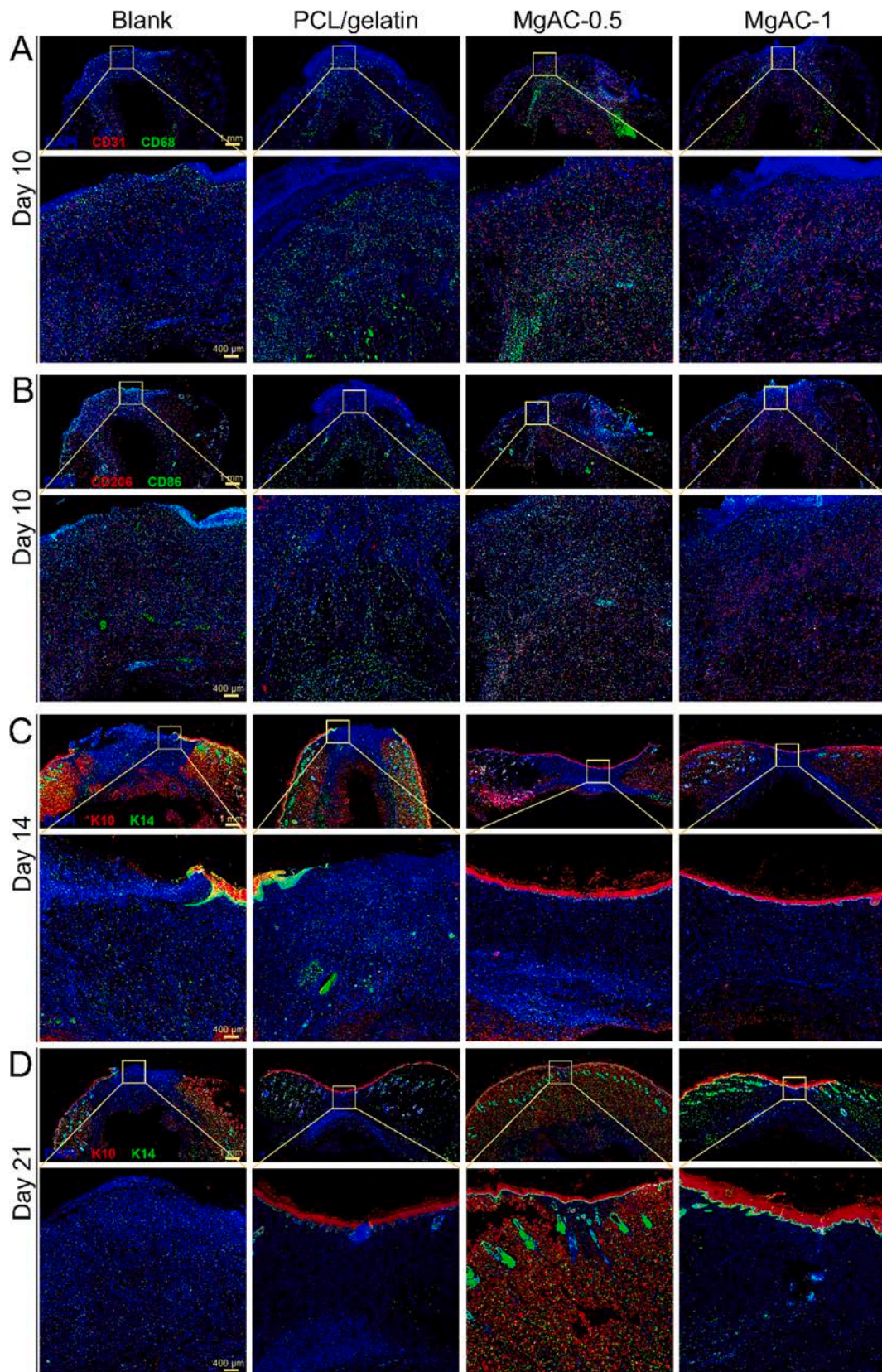


Fig. 9. Representative immunofluorescence images of wound tissue sections stained with CD31/CD68 (A) and CD206/CD86 (B) at day 10. Epidermal differentiation marker and epidermal basal cell marker of wounds at days 14 (C) and 21 (D) are immunofluorescent stained with K10 and K14, respectively, to assess epidermis maturation.

suggest that MgAC-incorporated membranes play a crucial role in restoring phenotypic transition in dysfunctional macrophages. It stimulates macrophage differentiation toward the M2 pro-healing phenotype and attenuates the inflammatory response, as evidenced by immunofluorescence staining results in diabetic rat wounds: CD86 (M1) fluoresces less area while CD206 (M2) has more fluorescence area (Fig. 9B). In addition, we show that the MgAC-0.5 membrane promotes rapid wound epithelialization. The MgAC-0.5 membrane-treated wound showed mature epidermis and the regenerated skin was completely covered by a K10-positive epidermal lining over the K14-positive epidermal basal layer (Fig. 9C-D). This is also associated with its anti-inflammatory activity (Fig. 9B) as observed in this study and our previous reports [32,33].

There are some limitations in the current study. Despite the good anti-inflammatory capacity of MgAC-incorporated membranes in this study and MgO-incorporated membranes in our previous reports [34,49], signaling pathways of this anti-inflammatory effect remains unknown. In addition, although STZ-induced diabetic rodents have been widely used to investigate diabetic wound healing, their repeatability and reliability remain unsure. Clinically relevant models of diabetic wounds would be better for the assessments in future studies.

5. Conclusions

Complete reaction of MgO nanoparticles with excess acetic acid to form MgAC significantly improved the physicochemical properties and bioactivity of the resulting electrospun membranes. This improvement is primarily owing to the chelate ring formed by the coordination of Mg²⁺ with gelatin. Although the MgAC-incorporated membranes show a slight compromise in antibacterial capacity, this method greatly increases the hydrophilicity and water adsorption capacity and tensile properties and prolongs Mg²⁺ release, as well as circumvents the MgO-hydrolysis caused pH elevation. The MgAC-incorporated membranes show good bioactivity in *in vitro* studies. In a diabetic rat full-thickness skin defect model, MgAC-incorporated membranes mitigated the inflammatory response, facilitated the M1 to M2 conversion of macrophages, and promoted granulation and mature epidermal tissue formation, enhancing diabetic wound healing. Future works of electrospun MgAC-incorporated membranes should focus on the elucidation of the signaling pathways underlying the magnesium-related immunomodulatory effects.

CRedit authorship contribution statement

Mingyue Liu: Formal analysis, Investigation, Visualization, Writing – original draft, Data curation. **Xiaoyi Wang:** Data curation, Formal analysis, Investigation, Visualization, Writing – original draft. **Binbin Sun:** Investigation, Writing – review & editing, Methodology. **Hongsheng Wang:** Formal analysis, Methodology. **Xiumei Mo:** Formal analysis, Methodology, Validation. **Mohamed EL-Newehy:** Methodology, Resources. **Meera Moydeen Abdulhameed:** Methodology, Resources. **Haochen Yao:** Resources, Supervision, Writing – review & editing. **Chao Liang:** Resources, Supervision, Validation. **Jinglei Wu:** Conceptualization, Formal analysis, Resources, Supervision, Validation, Writing – review & editing.

Declaration of competing interest

The authors declare no competing financial interest.

Data availability

Data will be made available on request.

Acknowledgments

The authors acknowledge support from Donghua University (2232023D-09), the Science and Technology Commission of Shanghai Municipality (19440741300), and the Doctor of Excellence Program (DEP) of the First Hospital of Jilin University (JDYYDEP-2022010). This project was also supported by Researchers Supporting Project Number (RSP2024R65), King Saud University, Riyadh, Saudi Arabia.

References

- [1] G.H. A, J.J.C.A. B, Bioresorbability, porosity and mechanical strength of bone substitutes: what is optimal for bone regeneration? *Injury* 42 (2) (2011) S22–S25.
- [2] K.G. A, A.C.S. B, A.V. B, D.A.L. A, 3D scaffolds in the treatment of diabetic foot ulcers: new trends vs conventional approaches, *Int. J. Pharm.* 599 (2021) 120423.
- [3] B. Hajhosseini, G.C. Gurtner, C.K. Sen, Abstract 48: And at Last, the Wound Is Healed... or, Is it?! In Search of an Objective Way to Predict the Recurrence of Diabetic Foot Ulcers, Plastic and Reconstructive Surgery–Global Open, 2019.
- [4] M. Chang, T.T. Nguyen, Strategy for treatment of infected diabetic foot ulcers, *Acc. Chem. Res.* 54 (5) (2021) 1080–1093.
- [5] S.A. Eming, T. Krieg, J.M. Davidson, Inflammation in wound repair: molecular and cellular mechanisms, *J. Invest. Dermatol.* 3 (2007) 127.
- [6] H.Y. Park, J.H. Kim, M. Jung, C.H. Chung, E.H. Choi, A long-standing hyperglycaemic condition impairs skin barrier by accelerating skin ageing process, *Exp. Dermatol.* 20 (12) (2011) 969–974.
- [7] J.E. Jelinek, Cutaneous manifestations of diabetes mellitus (letter), *Int. J. Dermatol.* 33 (9) (1994) 605–617.
- [8] T.A.N.M. Andrade, D.S. Masson-Meyers, G.F. Caetano, V.A. Terra, P.P.O. Ovidio, A. A. Jordão-Júnior, M.A.C. Frade, Skin changes in streptozotocin-induced diabetic rats, *Biochem. Biophys. Res. Commun.* (2017) 1154.
- [9] J.H. Kim, N.Y. Yoon, D.H. Kim, M. Jung, M. Jun, H.Y. Park, C.H. Chung, K. Lee, S. Kim, C.S. Park, Impaired permeability and antimicrobial barriers in type 2 diabetes skin are linked to increased serum levels of advanced glycation end-product, *Exp. Dermatol.* 27 (8) (2018) 815–823.
- [10] R. Blakytyn, E.B. Jude, Altered molecular mechanisms of diabetic foot ulcers, *Int J Low Extrem Wounds* 8 (2) (2009) 95–104.
- [11] M.C. Ryan, K. Lee, Y. Miyashita, W.G. Carter, Targeted disruption of the LAMA3 gene in mice reveals abnormalities in survival and late stage differentiation of epithelial cells, *J. Cell Biol.* 145 (6) (1999) 1309–1324.
- [12] Neil J. Vickers, Animal communication: when i'm calling you, will you answer too? *Curr. Biol.* 14 (2017) R713–R715.
- [13] D.G. Armstrong, A.J. Boulton, S.A. Bus, Supplement to: Diabetic Foot Ulcers and Their Recurrence, 2017.
- [14] B. Bruhn-Olszewska, A. Korzon-Burakowska, M. Gabig-Cimińska, P. Olszewski, J. J. Banecka, Molecular factors involved in the development of diabetic foot syndrome, *Acta Biochim. Pol.* 59 (4) (2012).
- [15] W. Ning, L. Wencong, C. Guodong, S. Shuwen, D. Qiteng, C. Zhiqiang, L. Xinglong, Z. Yingchun, Z. Ting, W. Yue, Y. Jiali, H. Bo, D. Chuanbo, Antibacterial, anti-inflammatory, rapid hemostasis, and accelerated repair by multifunctional metal–organic frameworks fibrous scaffolds for diabetic wounds, *Chem. Eng. J.* 477 (2023) 147262.
- [16] A. Nargess, S. Naser Sharifi, M. Reza Faridi, N. Saman Ahmad, Preparation and characterization of *Aloe vera* acetate and electrospinning fibers as promising antibacterial properties materials, *Mater. Sci. Eng. C* 94 (2019) 445–452.
- [17] Y. Jinke, W. Ke, Y. Deng-Guang, Y. Yaoyao, B. Sim Wan Annie, R.W. Gareth, Electrospun Janus nanofibers loaded with a drug and inorganic nanoparticles as an effective antibacterial wound dressing, *Mater. Sci. Eng. C* 111 (2020) 110805.
- [18] X. Xu, S. Wang, H. Wu, Y. Liu, F. Xu, J. Zhao, A multimodal antimicrobial platform based on MXene for treatment of wound infection, *Colloids Surf. B: Biointerfaces* 207 (2021) 111979.
- [19] L. Yu, S. Dou, J. Ma, Q. Gong, M. Zhang, X. Zhang, M. Li, W. Zhang, An antimicrobial peptide-loaded chitosan/polyethylene oxide nanofibrous membrane fabricated by electrospinning technology, *Front. Mater.* 8 (2021) 650223.
- [20] W. Wang, M. Liu, M. Shafiq, H. Li, R. Hashim, M. El-Newehy, H. El-Hamshary, Y. Morsi, X. Mo, Synthesis of oxidized sodium alginate and its electrospun biohybrids with zinc oxide nanoparticles to promote wound healing, *Int. J. Biol. Macromol.* 232 (2023) 123480.
- [21] Y. Zhang, J. Luo, Q. Zhang, T. Deng, Growth factors, as biological macromolecules in bioactivity enhancing of electrospun wound dressings for diabetic wound healing: a review, *Int. J. Biol. Macromol.* 193 (Pt A) (2021) 205–218.
- [22] J.S. Wrobel, B. Najafi, Diabetic foot biomechanics and gait dysfunction, *J. Diabetes Sci. Technol.* 4 (4) (2010) 833–845.
- [23] D. Pissuwan, S.M. Valenzuela, M.B. Cortie, Therapeutic possibilities of plasmonically heated gold nanoparticles, *Trends Biotechnol.* 24 (2) (2006) 62–67.
- [24] S. Wang, C. Yan, X. Zhang, D. Shi, L. Chi, G. Luo, J. Deng, Antimicrobial peptide modification enhances the gene delivery and bactericidal efficiency of gold nanoparticles for accelerating diabetic wound healing, *Biomater. Sci.* 6 (10) (2018) 2757–2772.
- [25] B. Pratibha, M. Himanshu, A. Mohammad, R. Alok, A.K. Teotia, K. Ashok, V. Nishith, Synthesis of yeast-immobilized and copper nanoparticle-dispersed carbon nanofiber-based diabetic wound dressing material: simultaneous control of glucose and bacterial infections, *ACS Appl. Bio Mater.* 1 (2) (2018) 246–258.

- [26] J. Edwards, N. Prevost, M. Santiago, T. Von Hoven, B. Condon, H. Qureshi, D. Yager, Hydrogen peroxide generation of copper/ascorbate formulations on cotton: effect on antibacterial and fibroblast activity for wound healing application, *Molecules* 23 (9) (2018).
- [27] G.N. Maity, P. Maity, I. Choudhuri, G.C. Sahoo, S. Mondal, Green synthesis, characterization, antimicrobial and cytotoxic effect of silver nanoparticles using arabinoside isolated from Kalmegh, *Int. J. Biol. Macromol.* 162 (2020).
- [28] C. Mao, Y. Xiang, X. Liu, Z. Cui, X. Yang, K.W.K. Yeung, H. Pan, X. Wang, P.K. Chu, S. Wu, Photo-inspired antibacterial activity and wound healing acceleration by hydrogel embedded with Ag/Ag@AgCl/ZnO nanostructures, *ACS Nano* 9 (2017) 9010–9021.
- [29] L. Shi, Y. Zhao, Q. Xie, C. Fan, J.N. Hilborn, J. Dai, D.A. Ossipov, Moldable hyaluronan hydrogel enabled by dynamic metal–bisphosphonate coordination chemistry for wound healing, *Adv. Healthc. Mater.* 5 (2017) 1700973.
- [30] P. Zhang, You Tang, Yaohui Shen, Hui Li, Jiankai Yi, Zhengfang Ke, He QinfeiXu, Copper-based metal-organic framework as a controllable nitric oxide-releasing vehicle for enhanced diabetic wound healing, *ACS Appl. Mater. Interfaces* 12 (16) (2020).
- [31] M.Y. Liu, R.L. Wang, J.J. Liu, W.X. Zhang, Z.N. Liu, X.X. Lou, H.L. Nie, H.S. Wang, X.M. Mo, A.I. Abd-Elhamid, R. Zheng, J.L. Wu, Incorporation of magnesium oxide nanoparticles into electrospun membranes improves pro-angiogenic activity and promotes diabetic wound healing, *Biomater. Adv.* 133 (2022) 112609.
- [32] M. Liu, R. Wang, J. Liu, W. Zhang, Z. Liu, X. Lou, H. Nie, H. Wang, X. Mo, A.I. Abd-Elhamid, R. Zheng, J. Wu, Incorporation of magnesium oxide nanoparticles into electrospun membranes improves pro-angiogenic activity and promotes diabetic wound healing, *Biomater. Adv.* 133 (2022) 112609.
- [33] M. Liu, W. Zhang, Z. Chen, Y. Ding, B. Sun, H. Wang, X. Mo, J. Wu, Mechanisms of magnesium oxide-incorporated electrospun membrane modulating inflammation and accelerating wound healing, *J. Biomed. Mater. Res. A* 111 (1) (2023) 132–151.
- [34] M. Liu, X. Wang, H. Li, C. Xia, Z. Liu, J. Liu, A. Yin, X. Lou, H. Wang, X. Mo, J. Wu, Magnesium oxide-incorporated electrospun membranes inhibit bacterial infections and promote the healing process of infected wounds, *J. Mater. Chem. B* 9 (17) (2021) 3727–3744.
- [35] X. Xie, D. Li, Y. Chen, Y. Shen, F. Yu, W. Wang, Z. Yuan, Y. Morsi, J. Wu, X. Mo, Conjugate electrospun 3D gelatin nanofiber sponge for rapid hemostasis, *Adv. Healthc. Mater.* 10 (20) (2021).
- [36] Cai Qun, He Ying, Huang Zhaolong, Bai Zhanhong, Li Xiuhuan, Coordination between gelatin and calcium and magnesium ions, *J. Honghe Univ.* 3 (6) (2005) 3.
- [37] L. Wang, Y. Zhong, C. Qian, D. Yang, J. Nie, G. Ma, A natural polymer-based porous sponge with capillary-mimicking microchannels for rapid hemostasis, *Acta Biomater.* 114 (2020) 193–205.
- [38] Y. Liang, C. Xu, F. Liu, S. Du, G. Li, X. Wang, Eliminating heat injury of zeolite in hemostasis via thermal conductivity of graphene sponge, *ACS Appl. Mater. Interfaces* 11 (27) (2019) 23848–23857.
- [39] T. Sinegre, A. Mazur, M.G. Berger, D. Milenkovic, A.F. Sapin, C. Morand, A. Lebreton, Epicatechin Impact on Primary Hemostasis, Coagulation and Fibrinolysis, 2016.
- [40] Méndez Rodrigo, Simon Rojano, Didier Mendez, Alexandre Lucor, Muriel Ranc, Kinetics of the coagulation cascade including the contact activation system: sensitivity analysis and model reduction, *Biomech. Model. Mechanobiol.* 4 (2019) 1139–1153.
- [41] W. Li, K. Xu, Y. Liu, X. Lei, X. Ru, P. Guo, H. Feng, Y. Chen, M. Xing, Hydrophobic polystyrene-modified gelatin enhances fast hemostasis and tissue regeneration in traumatic brain injury, *Adv. Healthc. Mater.* 12 (30) (2023) 2300708.
- [42] W.A. Ames, N. McDonnell, D. Potter, The effect of ionised magnesium on coagulation using thromboelastography, *Anaesthesia* 54 (10) (2015) 999–1001.
- [43] M. Liu, X. Wang, H. Li, C. Xia, J. Wu, Magnesium oxide incorporated electrospun membranes inhibit bacterial infections and promote healing process of infected wounds, *J. Mater. Chem. B* 9 (17) (2021) 3727–3744.
- [44] M. Ples, J. Glik, M. Misiuga, J. Skotnicka, M. Kawecki, M. Nowak, Chronic wounds and their treatment. Skin substitutes and allogeneic transplantations, *J. Orthopaed. Trauma Surg. Rel. Res.* 1 (38) (2016) 028–036.
- [45] R. Tiwari, G. Tiwari, A. Lahiri, R. Vadivelan, A.K. Rai, Localized delivery of drugs through medical textiles for treatment of burns: a perspective approach, *Adv. Pharm. Bull.* 2 (2021) 248–260.
- [46] K. Kaplani, S. Koutsi, V. Armenis, F.G. Skondra, N. Karantzelis, S.C. Tsaniras, S. Taraviras, Wound healing related agents: ongoing research and perspectives, *Adv. Drug Deliv. Rev.* 129 (2018) 242–253.
- [47] S.C. Davis, J. Li, J. Gil, J. Valdes, M. Solis, A. Higa, P. Bowler, The wound-healing effects of a next-generation anti-biofilm silver hydrofiber wound dressing on deep partial-thickness wounds using a porcine model, *Int. Wound J.* 15 (5) (2018) 834–839.
- [48] M. Liu, X. Wang, J. Cui, H. Wang, B. Sun, J. Zhang, B. Rolauffs, M. Shafiq, X. Mo, Z. Zhu, J. Wu, Electrospun flexible magnesium-doped silica bioactive glass nanofiber membranes with anti-inflammatory and pro-angiogenic effects for infected wounds, *J. Mater. Chem. B* 11 (2) (2023) 359–376.
- [49] X. Liu, X. He, D. Jin, S. Wu, H. Wang, M. Yin, A. Aldalbahi, M. El-Newehy, X. Mo, J. Wu, A biodegradable multifunctional nanofibrous membrane for periodontal tissue regeneration, *Acta Biomater.* 108 (2020) 207–222.
- [50] F. Gueraud, M. Atalay, N. Bresgen, A. Cipak, P.M. Eckl, L. Huc, I. Jouanin, W. Siems, K. Uchida, Chemistry and biochemistry of lipid peroxidation products, *Free Radic. Res.* 44 (10) (2010) 1098–1124.
- [51] S. Schreml, R.M. Szeimies, L. Prantl, S. Karrer, M. Landthaler, P. Babilas, Oxygen in acute and chronic wound healing, *Br. J. Dermatol.* 163 (2) (2010) 257–268.
- [52] J.Z. Dai, X.T. Zhang, Y.M. Wang, H. Chen, Y.M. Chai, ROS-activated NLRP3 inflammasome initiates inflammation in delayed wound healing in diabetic rats, *Int. J. Clin. Exp. Pathol.* 10 (9) (2017) 9902–9909.